

# UC Santa Barbara

## UC Santa Barbara Previously Published Works

### Title

Infrasound Signal Detection and Back Azimuth Estimation Using Ground-Coupled Airwaves on a Seismo-Acoustic Sensor Pair

### Permalink

<https://escholarship.org/uc/item/00d940gg>

### Journal

Journal of Geophysical Research: Solid Earth, 123(8)

### ISSN

2169-9313

### Authors

McKee, Kathleen

Fee, David

Haney, Matthew

et al.

### Publication Date

2018-08-01

### DOI

10.1029/2017jb015132

### Copyright Information

This work is made available under the terms of a Creative Commons Attribution-NonCommercial-NoDerivatives License, available at <https://creativecommons.org/licenses/by-nc-nd/4.0/>

Peer reviewed

RESEARCH ARTICLE

10.1029/2017JB015132

Key Points:

- We present a method to use a nearly co-located seismic and acoustic sensor to detect acoustic waves and determine a unique back azimuth
- Application of our method to synthetic and recorded data produces back azimuth results similar to traditional array processing
- Successful application of this method requires adequate sensor separation, sample rate, and a three-component seismometer

Supporting Information:

- Supporting Information S1
- Data Set S1
- Data Set S2
- Data Set S3
- Data Set S4
- Data Set S5
- Data Set S6
- Data Set S7
- Data Set S8
- Data Set S9
- Data Set S10
- Data Set S11
- Data Set S12
- Data Set S13
- Data Set S14
- Data Set S15
- Data Set S16
- Data Set S17
- Data Set S18
- Data Set S19

Correspondence to:

K. McKee,  
kfmckee@alaska.edu

Citation:

McKee, K., Fee, D., Haney, M., Matoza, R. S., & Lyons, J. (2018). Infrasound signal detection and back azimuth estimation using ground-coupled airwaves on a seismo-acoustic sensor pair. *Journal of Geophysical Research: Solid Earth*, 123, 6826–6844. <https://doi.org/10.1029/2017JB015132>

Received 19 OCT 2017

Accepted 17 JUL 2018

Accepted article online 27 JUL 2018

Published online 22 AUG 2018

# Infrasound Signal Detection and Back Azimuth Estimation Using Ground-Coupled Airwaves on a Seismo-Acoustic Sensor Pair

Kathleen McKee<sup>1,2</sup> , David Fee<sup>1</sup> , Matthew Haney<sup>3</sup> , Robin S. Matoza<sup>4</sup> , and John Lyons<sup>3</sup> 

<sup>1</sup>Alaska Volcano Observatory, Geophysical Institute, University of Alaska Fairbanks, Fairbanks, AK, USA, <sup>2</sup>Now at Department of Terrestrial Magnetism, Carnegie Institution for Science, Washington, DC, USA, <sup>3</sup>Alaska Volcano Observatory, U.S. Geological Survey Volcano Science Center, Anchorage, AK, USA, <sup>4</sup>Department of Earth Science and Earth Research Institute, University of California, Santa Barbara, CA, USA

**Abstract** We present a new infrasonic signal detection and back azimuth determination technique that requires just one microphone and one three-component seismometer. Ground-coupled airwaves (GCAs) occur when an incident atmospheric acoustic wave impinges on the ground surface and is partially transmitted as a seismic wave. GCAs are commonly detected hundreds of kilometers away on seismic networks and are observed to have retrograde particle motion. Horizontally propagating acoustic waves and GCAs have previously been observed on collocated infrasound and seismic sensor pairs as coherent with a 90° phase difference. If the sensors are spatially separated, an additional propagation-induced phase shift is present. The additional phase shift depends on the direction from which the acoustic wave arrives, as each back azimuth has a different apparent distance between the sensors. We use the additional phase shift, the coherence, and the characteristic particle motion on the three-component seismometer to determine GCA arrivals and their unique back azimuth. We test this technique with synthetic seismo-acoustic data generated by a coupled Earth-atmosphere 3-D finite difference code, as well as three seismo-acoustic data sets from Mount St. Helens, Mount Cleveland, and Mount Pagan volcanoes. Results from our technique compare favorably with traditional infrasound array processing and provide robust GCA detection and back azimuth determination. Assuming adequate station spacing and sampling, our technique provides a new and robust method to detect infrasonic signals and determine their back azimuth, and may be of practical benefit where resources are limited and large sensor networks or arrays are not feasible.

## 1. Introduction

A common goal of the infrasound community is to detect and determine the direction (back azimuth) from which a signal originated. Typical infrasonic array deployments consist of at least three, and usually four to eight, infrasonic microphones distributed on the ground surface to detect and determine the back azimuth of low-frequency acoustic waves (Christie & Campus, 2009). Green (2015) shows examples of International Monitoring System (IMS) infrasound arrays deployed with apertures ranging from 1 to 4 km as of March 2014. Traditional methods for detecting and determining back azimuth to a source are executed in two steps (Olson & Szuberla, 2008). First, frequency-wavenumber (F-k) analysis (similar to delay and sum beamforming in the time domain) or least squares estimation of a plane wave arrival (Olson & Szuberla, 2005) is used to determine the back azimuth for each window of data. The waves are assumed to be planar. Then methods such as Fisher's F-statistic (Olson & Szuberla, 2008; Smart & Flinn, 1971) or mean cross-correlation maxima (MCCM) (Lee et al., 2013) are used to assess whether the data analyzed in each window are highly correlated and can be deemed a detection. The Progressive Multi-Channel Correlation (PMCC) algorithm combines detection and characterization of a signal. PMCC cross correlates the data from array subsets (triads), computes time delays, and uses the sum of time delays between unique sensor pairs within a triad to establish a closure relationship (Cansi, 1995; Cansi & Klinger, 1997). The analysis progresses as triads are combined to create larger groups. If the closure relationship for a given window of data holds through combining triads, then the signal back azimuth and velocity estimate becomes increasingly accurate. PMCC is applied for a given time window across multiple-frequency bands and then advanced to the next window. These methods are conducted using arrays of three or more infrasonic microphones.

A frequently observed phenomenon in infrasonic wave propagation is when an incident acoustic wave traveling through the atmosphere encounters the Earth's surface and part of the wave energy is transferred

to the ground as a seismic wave, known as a ground-coupled airwave (GCA). GCAs from a variety of sources including volcanoes, bolides, meteors, and explosions are regularly detected on seismometers (De Angelis et al., 2012; Edwards et al., 2007; Fee et al., 2016, 2017; Ichihara et al., 2012; Johnson & Malone, 2007; Langston, 2004; Matoza & Fee, 2014; Nishida & Ichihara, 2015; Smith et al., 2016; Tauzin et al., 2013; Walker et al., 2010). Here we present a method to determine the back azimuth to an acoustic source detected on a nearly collocated three-component seismometer and infrasonic microphone. This method requires less instrumentation than a traditional infrasonic array and provides information not available from the seismometer alone. In this manuscript, we describe the GCA back azimuth determination (BAD) method, test it using synthetic data from a coupled Earth-atmosphere 3-D finite difference code, and then apply it successfully to three volcanic data sets: Mount St. Helens, USA; Mount Cleveland, USA; and Mount Pagan, Commonwealth of the Northern Mariana Islands (CNMI). These applications are followed by a discussion of best practices for using the method. It is well established that nearly collocated seismo-acoustic sensors can be used for robust detections of volcanic activity by means of cross correlation (Ichihara et al., 2012; Nishida & Ichihara, 2015) or coherence (Fee et al., 2017; Matoza et al., 2018; Matoza & Fee, 2014) analysis. To our knowledge, back azimuth, an important parameter in geophysical signal detection and characterization, has not been determined for an acoustic source using the time delay between a nearly collocated seismometer and infrasound sensor alone. It has been determined for seismic sources using particle motions, but we discuss later how this is often very difficult and that our method is more robust. Additionally, the synthesis of particle motion, coherence, and time delays between nearly collocated sensors has not been performed before.

## 2. Background

In the case where an incident acoustic wave encounters the ground nearly parallel to the surface, referred to as “grazing incidence” (Ben-Menahem & Singh, 2000), the wave couples to the ground as it propagates through the atmosphere, thus giving an apparent velocity of  $\sim 343$  m/s (the speed of sound in the atmosphere). The seismic particle motion is retrograde and elliptical since it is a guided interface wave and it is detectable on a three-component seismometer (Edwards et al., 2007; Ichihara et al., 2012). As the particle motion is retrograde and elliptical, it is recorded on the vertical and horizontal components and points, roughly, back to the source. If the angle of incidence is closer to vertical, the incident pressure wave can induce a  $P$  wave and subsequently  $S$  and Rayleigh waves, which travel through the subsurface at their respective speeds. This was clearly observed with the breakup of the Chelyabinsk meteor (Tauzin et al., 2013). The focus of this manuscript is the more typical case where atmospheric pressure waves couple to the Earth at angles near  $90^\circ$  from vertical.

Recent work has shown that in acoustic time series data, signals may be distinguished from wind noise by cross correlating the acoustic data with that from a nearly collocated seismometer (Ichihara et al., 2012). The key factor that makes this possible is separating the microphone and seismometer by a distance greater than the correlation length of wind noise. In the example presented by Ichihara et al. (2012) at Asama Volcano, the microphone was attached to a 4-m-long pipe to connect it to the atmosphere, effectively separating the seismic and infrasonic sensors. The separation distance required is dependent upon the frequency of interest and wind speed. Wind noise recorded on two sensors will correlate at a given frequency,  $f$ , if the interstation distance is one third or less than the wind eddy size ( $v/f$ ), where  $v$  is the wind speed (Shields, 2005; Wilson et al., 2007). By separating the sensors by more than this distance the incident pressure wave will still correlate because the acoustic wavelengths at the same frequency,  $(c/f)$ , where  $c$  is speed of sound, are much longer. For example, an infrasonic wavelength at 1 Hz is  $\sim 343$  m and eddy size for an  $\sim 3$  m/s wind at the same frequency is 3 m.

Ichihara et al. (2012) propose that the dominant terms in the seismo-acoustic cross-correlation function are the incident acoustic pressure wave,  $p_{in}$ , and the vertical ground velocity generated by the acoustic pressure wave,  $H_{pw}p_{in}$ , where  $H_{pw}$  is the transfer coefficient. From Ben-Menahem and Singh (2000), assuming that the incident acoustic wave propagates along the surface, the transfer coefficient can be estimated using

$$H_{pw} = \frac{e^{-i\pi/2} c_a \lambda + 2\mu}{2(\lambda + \mu) \mu}$$

where  $\lambda$  and  $\mu$  are the Lamé parameters of the solid medium and  $c_a$  is the acoustic phase velocity. If the

airwave arrives nearly horizontal to the ground surface, then the apparent velocity will be equal to the sound speed. The  $e^{-i\pi/2}$  indicates that the vertical ground velocity generated by the acoustic pressure wave has a  $90^\circ$  phase shift relative to the acoustic pressure wave. The  $90^\circ$  phase shift corresponds to the case when the sensors are collocated. As mentioned, the ability to distinguish signals requires that the sensors be separated such that wind noise is uncorrelated and incoherent. This separation creates an additional time shift between the signals, which must be corrected in order for the  $90^\circ$  phase to become apparent (Matoza & Fee, 2014). The additional phase can be removed if the sensor pair geometry, back azimuth to the source, and apparent velocity are known. When the seismic and acoustic data are cross correlated this shift is present as a time delay and may indicate coherent acoustic waves as opposed to noise. In applying this method, Ichiyama et al. (2012) filtered the seismic and acoustic waveforms from 1 to 7 Hz. The lower and upper bounds were chosen to ensure that given the intersensor spacing wind noise would not correlate and to avoid the influence of local topography, respectively (Ichiyama et al., 2012). One challenge with the cross-correlation method is that the frequency band in which two signals correlate may be narrow and is unknown a priori. This requires a systematic search over many different frequency bands to find the one in which the signals correlate. To address this, Matoza and Fee (2014) looked at the coherence spectra of the unfiltered seismic and acoustic data to find frequencies at which the waveforms correlate.

Coherence provides an intuitive measure of how similar two time series are with respect to their frequency content, with 0 being dissimilar and 1 being identical. The coherence spectrogram is a measure of this similarity taken in windows through time (similar to a spectrogram). In this same manner, Matoza and Fee (2014) analyzed the phase spectrogram, which is the phase between two time series at different frequencies also taken in windows through time. Matoza and Fee (2014) analyzed GCAs on nearly collocated acoustic and seismic stations and looked at the coherence and phase delays in three different data sets: Mount St. Helens, Washington, USA; Tungurahua, Ecuador; and Redoubt, Alaska, USA. The method worked well with the Mount St. Helens data, detecting  $\sim 2,000$  s of coherent signal above the background seismic activity. Once the phase shift was corrected for the offset between stations, the phase difference between the seismic and acoustic was near  $90^\circ$ . At Tungurahua, the method again detected coherent signal, but it did not for the Redoubt data set. The incoherence found in the Redoubt data is likely due to distinct acoustic and seismic sources (Matoza & Fee, 2014). This highlights the fact that coupling does not always occur or is not always dominant/detectable. GCAs from the 2016 eruption at Pavlof Volcano, USA, were also identified on EarthScope Transportable Array (TA) sites in Alaska using coherence (Fee et al., 2017).

We note that there are a variety of factors that influence the ability of an acoustic wave to couple to the ground. Frequency-dependent, near-surface geological site effects (as the transfer coefficient equation previously stated is for a homogeneous, solid half-space; Ben-Menahem & Singh, 2000), incidence angle, and range dependence (because higher-frequency content is preferentially attenuated) are all thought to be important influences. Other factors include seismometer burial depth, topography, frequency content, and observation distance (Edwards et al., 2007; Madhus et al., 2005).

### 3. Infrasonic Source BAD Method

Here we describe our methodology to determine the back azimuth of an incident acoustic wave recorded on a seismo-acoustic sensor pair. Details on the method to distinguish the infrasonic component of the seismic record (i.e., GCA) can be found in the supporting information along with an infographic (S1). The intersensor distance,  $d$ , and the azimuth from seismometer to the infrasonic microphone,  $\beta$ , are determined from the locations of the sensors (Figure 1). We define azimuth as the angle measured clockwise from north ( $0^\circ$ ) from one location to another and back azimuth as the direction from which a wave originated, again measured clockwise from north. We can determine the times and frequencies in which the seismic and acoustic waveforms are similar by evaluating the coherence. If the seismic trace is dominated by a GCA, shown by the seismo-acoustic coherence, the phase should be  $90^\circ$ . This means the observed phase,  $\rho$ , is a sum of the  $90^\circ$  phase and the additional phase from the sensor separation,  $\rho_{d_0}$ . To determine the back azimuth to the source, we need to find the time shift that minimizes the additional phase from the sensor separation. However, this time shift does not determine a unique back azimuth as the same apparent distance, and thus time shift, can be found about the line connecting the seismometer and microphone,  $d$  (Figure 1, Step 1). This nonunique

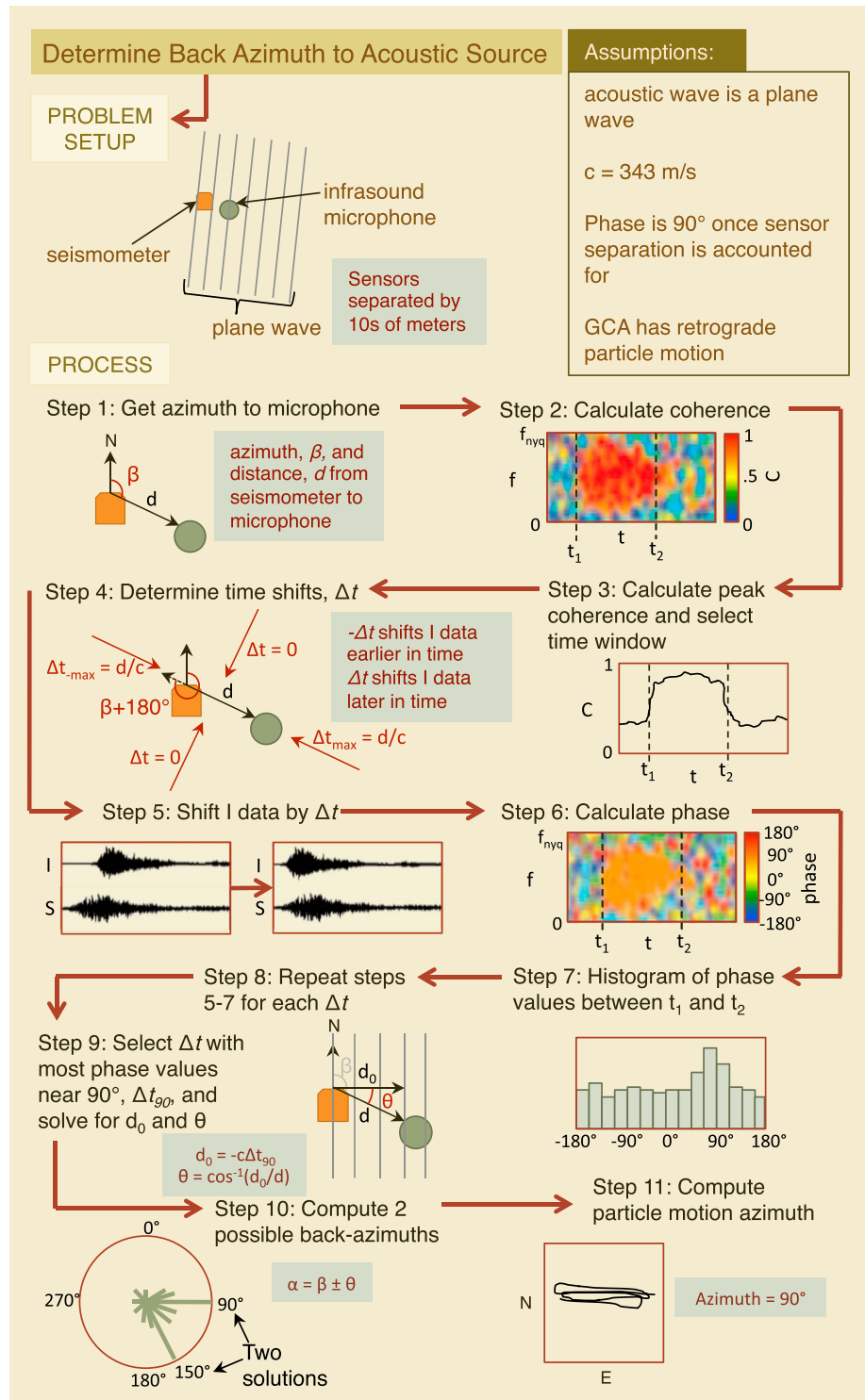


**Figure 1.** Infographic illustrating the steps to determine the back azimuth to an acoustic source that has been recorded by newly collocated seismic and infrasound sensors. See text for more details.

solution exists for two-element infrasound arrays as well. Thus, additional information is needed to resolve a unique solution, such as the particle motion from the seismometer. As GCAs normally have retrograde particle motion in the direction of propagation (Aki & Richards, 2002; Ben-Menahem & Singh, 2000; Edwards et al., 2007, 2008), a rough estimate of the back azimuth can be calculated (Edwards et al., 2007;

Montalbetti & Kanasewich, 1970; Neuberg & Pointer, 2000; Vidale, 1986; Wang & Kaveh, 1985) and used to determine a unique solution from the multiple back azimuths derived in previous steps. Figure 1 and the following steps describe this method in more detail.

In order to determine the back azimuth from a seismo-acoustic sensor pair, we assume that the incident acoustic pressure wave is a plane wave traveling at the speed of sound in the atmosphere. For MSH and Pagan, we assume an air temperature of 20 °C with negligible wind, which gives a sound speed of ~343 m/s. We assume a cooler air temperature (−10 °C) and lower sound speed (325 m/s) for the Mount Cleveland examples as the sensors are deployed at high latitudes and the explosions occurred in the winter months. We also assume that the wave couples to the ground and the phase is 90° when the sensors are collocated. This assumption is supported by theory (Ben-Menahem & Singh, 2000) and observations (Ichihara et al., 2012; Matoza & Fee, 2014). Seismic and acoustic data are preprocessed by removing the instrument responses and high-pass filtering above 20 s to remove long-period noise and drift.

#### Step 1: Get azimuth to microphone

We then calculate the azimuth from seismometer to microphone,  $\beta$  (Figure 1, Step 1). For simplicity, and to maintain consistency throughout, we have chosen to apply this method relative to the seismometer, such that azimuths are relative to the seismometer's location and north. The distance from the seismometer to the microphone is  $d$ .

#### Step 2: Calculate coherence

We calculate the coherence spectrogram by taking coherence of the infrasound and seismic data in windows with 90% overlap (Figure 1). Window lengths are dependent on the signal length of interest. We chose window lengths to capture multiple waveform periods for broadband data and to allow for many windows over the duration of the signal. For example, we use a 4-s window for the synthetic and Cleveland data sets as the signals are ~4–5 s in duration, but we use a 10-s window for the MSH and Pagan data sets, which are ~1,850 and ~30 s in duration, respectively.

#### Step 3: Calculate peak coherence and select time window

Here we calculate the peak coherence and use it to select a time window for further analysis (Figure 1). For each time step (displayed as a column) in the coherence spectrogram, we take windows of the coherence relative to frequency with a 90% overlap and determine the mean for each window of frequency from zero to the Nyquist frequency. We use a window of ~1 Hz for the synthetic data and ~2 Hz for the MSH, CLCO, and Pagan data. Then we save the maximum mean coherence value from those windows and repeat for each coherence time step. Peak coherence values above a set threshold indicate coherent GCA arrivals; here we use a threshold of 0.8.

#### Step 4: Prepare time shifts

In this step, we prepare the set of time shifts,  $\Delta t$ , to search over for the two back azimuth solutions (Figure 1). We search from  $-\Delta t_{\max} = -d/c$  to  $\Delta t_{\max} = d/c$ , where each  $\Delta t$  has two possible back azimuths and the range covers azimuths from 0° to 360°. We use an interval step of  $dt/4$  as this gave the best results for the three data sets evaluated, where  $dt$  is the time between samples.

#### Step 5: Shift infrasound data by $\Delta t$

Now we search for possible back azimuths by calculating the phase spectrogram for each time shift. To do this we shift the infrasound data by the first  $\Delta t$  in the set of possible time shifts,  $-\Delta t_{\max}: dt/4: \Delta t_{\max}$  (Figure 1).

#### Step 6: Calculate phase

Calculate the phase spectrogram between the seismic and time-shifted infrasound trace (Figure 1).

#### Step 7: Histogram of phase values between $t_1$ and $t_2$

To analyze the phase values, take a histogram of phase values between  $t_1$  and  $t_2$  from zero to the Nyquist frequency (Figure 1). We set our bin widths at 3° from −180° to 180°. Next we save the number of values in bins closest to 90°; the bins of interest for our bin width are 87° to 90° and 90° to 93°.

#### Step 8: Repeat Steps 5–7 for each $\Delta t$

As each  $\Delta t$  corresponds to two back azimuths, searching from  $-\Delta t_{\max}$  to  $\Delta t_{\max}$  is effectively a search over the possible back azimuths from  $0^\circ$  to  $360^\circ$ .

Step 9: Select  $\Delta t$  with most phase values near  $90^\circ$ ,  $\Delta t_{90}$ , and solve for  $d_0$

The  $\Delta t$  with the most values in the bins closest to  $90^\circ$ ,  $\Delta t_{90}$ , is the  $\Delta t$  that minimizes the additional phase due to the sensor separation. For a given travel time difference between two sensors without a known first arrival, there are four possible back azimuths. We eliminate two of the four by the sign of  $\Delta t$ , in other words by searching from  $-\Delta t$  to  $\Delta t$ . If  $\Delta t$  is negative, then there is an infrasonic first arrival and if  $\Delta t$  is positive, then there is a seismic first arrival. That is, if  $-\Delta t$ , then the infrasound data have to be shifted later in time relative to the seismic data, and vice versa. We then use  $\Delta t_{90}$  to calculate the apparent distance,  $d_0$ , (Figure 1). Next we compute  $\theta$ , the angle between  $d$  and  $d_0$ , which is ultimately the angle between  $d$  and  $\alpha$ , the direction from which the wave arrives:  $\theta = \cos^{-1}\left(-c\Delta t/d\right)$ .

Step 10: Compute two possible back azimuths

The possible back azimuths,  $\alpha$ , are  $\alpha = \beta \pm \theta$ , where  $\beta$  is the azimuth from seismometer to microphone. For the example illustrated in Figure 1, Steps 9 and 10, there is an infrasonic first arrival, so  $\alpha = \beta \pm \theta$ . If it was a seismic first arrival, then the back azimuths would be  $\alpha = \beta \pm 180 \pm \theta$ . We recalculate  $\alpha$  to range from  $0^\circ$  to  $360^\circ$ .

Step 11: Compute particle motion azimuth

To find a unique back azimuth solution, we use the particle motion on the seismometer (Figure 1). We employ the Coherency Matrix method (Vidale, 1986) to automatically compute the particle motion azimuth through time and in our testing find that it performs better than the covariance method (Montalbetti & Kanasevich, 1970; Wang & Kaveh, 1985). We use a window length of 4 s for the synthetic and Cleveland data and 10 s for MSH and Pagan to maintain consistency with the coherence and phase spectrogram calculations. Next, we select the particle motion back azimuth at the time of peak coherence, compare it to the  $\Delta t$  search results, and select the back azimuth search result closest to the particle motion solution. The search result that is closest to the particle motion solution is the unique back azimuth to the source. To check the particle motion is elliptical, we integrate the three-component seismic data to get displacement and then plot 1 s of Z versus E, Z versus N, E versus N, and Z versus E versus N (3-D plot) starting at the time of peak coherence. The particle motion analysis step gives the impression that particle motion alone could be used to determine the back azimuth to an infrasonic source, but timing and noise prevent this. The coherence analysis between the seismic and infrasonic traces provides the timing for when to look at the seismic particle motion. Back azimuths determined using particle motion analysis from a single three-component seismometer can have high variance, which can be reduced by deploying an array of three-component sensors in order to increase the signal-to-noise ratio (SNR) through beam-forming (Jurkevics, 1988). Given these factors, we simply use the particle motion to determine the unique solution from the two back azimuth solutions determined in the  $\Delta t$  search.

#### 4. Data

We use four data sets to evaluate the efficacy of our method: a synthetic data set generated using finite differences with a 40 -m resolution digital elevation model of Mount Pagan Volcano, CNMI; recorded data from Mount St. Helens Volcano; recorded data from Mount Cleveland Volcano; and recorded data from Mount Pagan Volcano. Figure 2 shows the synthetic data used, which were generated by a coupled Earth-atmosphere 3-D finite difference code (Haney et al., 2009). The source was a Ricker wavelet with center frequency of 1.4 Hz, which gives an effective bandwidth of 0.08 to 3.87 Hz. As in Lyons et al. (2016), the source location is just below the vent of Mount Pagan and the material properties are as follows:  $V_p = 3,500$  m/s,  $V_s = 2,000$  m/s in the Earth and a density of  $2,700$  kg/m<sup>3</sup>. The seismometer is 3,000 m to the southwest, where the actual station PGBF is located. The synthetic seismic wavefield is sampled at 40 m nodes in the vertical plane extending 160 m above and below the seismometer. The synthetic acoustic wavefield is sampled at the same vertical nodes in addition to horizontal nodes at 20, 40, 60, and 80 m to the south, such that there is a 2-D plane of nodes. We used the synthetic seismo-acoustic data from the node two intervals above the seismometer to avoid irregularities in coupling along the Earth-atmosphere boundary (Matoza et al., 2009).

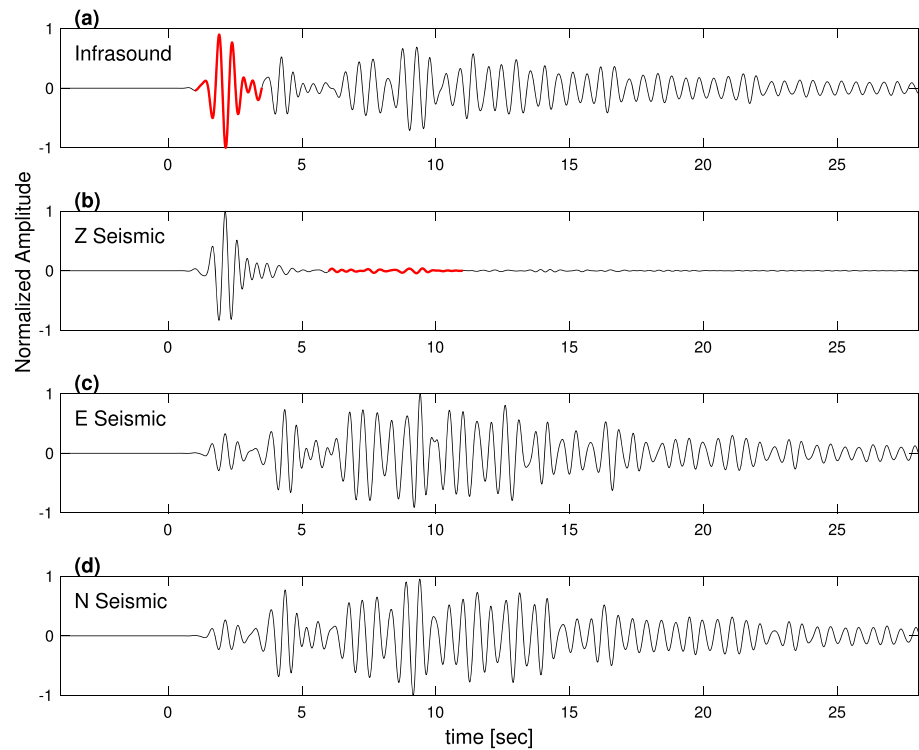


**Figure 2.** Synthetic, normalized, and unfiltered waveforms generated using a coupled Earth-atmosphere 3-D finite difference code: (a) infrasound, (b) vertical seismic, (c) east seismic, (d) north seismic. The explosion seismic wave reaches the seismometer at 4 s. This wave also generates an air-coupled ground-wave (red portion in (a)). The airwave and GCA (red portion in (b)) arrives at ~6 s. The notable wave packet in (c) and (d) from ~3 to 5 s is the Rayleigh wave diffracting into an airwave at the caldera wall. It is less noticeable in b because each trace has been normalized relative to their respective maximum value. This same wave packet is present in the infrasound trace as a Rayleigh air-coupled ground-wave. Figure S2 shows map view time slices from  $t = 0.5$  to 6.0 s of this wave packet passing by PGBF.

We use the seismo-acoustic data recorded at the Coldwater (CDWR) array from the 8 March 2005 phreatic explosion at Mount St. Helens Volcano (Matoza et al., 2007). CDWR had a four-element, broadband (0.01–17 Hz) centered-triangular infrasound array of MB2000 aneroid microbarometers with an approximate aperture of 100 m. A Güralp CMG-40T broadband seismometer (0.033–50 Hz) was deployed a few meters from the central microbarometer. The seismo-acoustic data were sampled at 40 Hz. As in Matoza and Fee (2014), we use the second element of the infrasound array for GCA analysis, which is northeast of the seismometer by 14 m N and 51 m E. Only the vertical and radial seismic channels were recorded at CDWR. The peak seismic and acoustics amplitudes are  $\sim 2 \mu\text{m/s}$  and  $\sim 0.5\text{--}1 \text{ Pa}$ , respectively, at 13.4 km.

For the Mount Cleveland data set, we use two explosions recorded at the CLCO seismo-acoustic station on 13 December 2017 and 2 March 2018. CLCO was installed by the Alaska Volcano Observatory (AVO) in August 2014 and has a three-component, CMG-6TD broadband seismometer (0.03–100 Hz) and a five-element, collocated infrasound array. The infrasound array elements have VDP-5 differential pressure transducers (Thelen & Cooper, 2015) with a flat response between 0.0125 and 25 Hz and a sensitivity of 16.7 mV/Pa. Explosions at Mount Cleveland are usually high amplitude and short duration, lasting a few seconds. The peak seismic and infrasonic amplitudes for the 13 December 2017 explosion are  $40.9 \mu\text{m/s}$  and  $69.3 \text{ Pa}$ , respectively, at 15.4 km.

Lastly, for the Mount Pagan data set, we use an explosion recorded on 26 July 2013 at the PGBF seismo-acoustic station installed by the U.S. Geological Survey in June 2013 (Lyons et al., 2014). PGBF has a three-component, Güralp 6TD intermediate band (0.033–50 Hz) seismometer and a six-element, collocated infrasound array of VDP-10 differential pressure transducers (Thelen & Cooper, 2015) with flat responses between 0.0125 and 25 Hz and a sensitivity of 10 mV/Pa. At the time of the explosion studied here, Pagan activity was dominated by continuous degassing from the summit vent that generated

long-period seismic events and very-long-period infrasound events (10–50 per hour); explosions were infrequent (Lyons et al., 2014, 2016). The seismo-acoustic energy from the explosion is peaked between 0.25 and 5 Hz with signals lasting 20–30 s. Acoustic amplitudes are  $\sim 1\text{--}2$  Pa at  $\sim 3$  km with seismic amplitudes at  $\sim 6$   $\mu\text{m/s}$ .

## 5. Results

### 5.1. Synthetic Data Set

We first apply our method to determine the back azimuth to an infrasonic source using the synthetic data described in section 4. Figure 3 shows the (a) synthetic infrasound and seismic waveforms with the sensors separated by 60 m, (b) coherence spectrogram, (c) peak coherence, (d) raw phase spectrogram, and (e) time-shifted phase spectrogram. Note the high coherence values from  $-0.5$  to  $\sim 3.5$  s and  $\sim 6$  to 11 s, which are also highlighted in the peak coherence through time (Figure 3c). The initial high coherence is between the seismic explosion signal and the air-coupled ground wave; the second window is during the GCA. We added pink noise to the synthetics to eliminate high-coherence values prior to the explosion signal when the traces were both zero. Figure 3d shows the phase between the seismic and infrasonic traces, and Figure 3e shows the phase between the seismic and time-shifted infrasound data, where the time shift is defined as the one with the most phase values near  $90^\circ$ . Note the phase from Figures 3d to 3e shifts to dark orange around  $\sim 6\text{--}12$  s, closer to  $90^\circ$ . To avoid the high coherence from  $\sim -0.5$  to 3 s between the seismic explosion signal and the air-coupled ground wave, we applied our method to the data from 4 to 22 s (Figure 4). Figure 4a shows the histograms for each time shift, where each horizontal row is a time shift, each column is a phase value, and the color scale represents the number of values in each bin. The dotted white line denotes  $90^\circ$  phase. Figure 4b shows the two back azimuths in polar coordinates (rose diagram) associated with each time shift on the y axis of Figure 4a. The length of each bar in the rose diagram indicates the total number of phase values in the bins close to  $90^\circ$  (i.e.,  $87^\circ$  to  $90^\circ$  and  $90^\circ$  to  $93^\circ$ ; Figure 4b). As the time shifts each have two associated back azimuths, the rose diagram in Figure 4b is symmetric about the azimuth line,  $\beta$ . The two principal back azimuths for the synthetic Pagan data are  $50^\circ$  and  $310^\circ$ . The coherency matrix method particle motion analysis finds a direction of  $46.0^\circ$  at the time of peak coherence, thereby suggesting  $50^\circ$  as the back azimuth to source (via the phase shift in Figure 4b). The actual back azimuth to the synthetic Pagan source is  $51.4^\circ$  (solid black arrow in Figure 4c). To check the particle motion analysis and our assumption that the GCA has elliptical particle motion, we plot and analyze 1 s of 3-D displacements (Figure 5). The particle motion is elliptical and retrograde given the back azimuth determined.

In addition to the 60 m sensor separation, we also tested the method at  $d = 20, 40,$  and  $80$  m. The search parameters and results are in Tables 1 and 2, respectively. For a GCA with energy between 0.2 and 2.7 Hz, the 80 m separation had a back azimuth closest to the actual.

### 5.2. Mount St. Helens

We apply the method to a previously studied data set: the MSH 8 March 2005 phreatic explosion. Figure 6 shows the same analysis as Figure 3 but for MSH. As shown in Matoza and Fee (2014), the seismic and infrasonic waveforms are more similar when filtered from 5 to 19 Hz (Figure 6a) and are coherent at higher frequencies (Figure 6b). The peak coherence is above the 0.8 threshold from  $\sim 150$  to 2,000 s (Figure 6c). Figure 6d shows the original phase estimates flip between  $-180^\circ$  and  $180^\circ$ , and Figure 6e shows the phase after the time shift found in the search is applied to the infrasound trace, which is close to  $90^\circ$ . Figure 7a shows a visual representation of the search results with phase from  $-180^\circ$  to  $180^\circ$  across the x axis and each time shift along the y axis. The  $\Delta t$  with the most values near  $90^\circ$  is  $\Delta t_{90} = 0.025$  in this example. We translate the time shifts to back azimuths (Figure 7b), which indicates that there are two prominent back azimuths at  $155^\circ$  and  $354^\circ$ . Unfortunately, this data set only has the vertical and radial channels of seismic data, so we are unable to apply the particle motion analysis to find a unique solution. However, infrasound array processing results from Matoza and Fee (2014) found a back azimuth of  $153^\circ$  and the actual back azimuth is  $154^\circ$ , which is very close to one of our GCA BAD estimates. Matoza and Fee (2014) note a signal with high coherence prior to the MSH phreatic explosion that does not have  $90^\circ$  phase, and PMCC finds that it has a different back azimuth. We applied our technique to that signal, and one of our nonunique search results is within the back azimuth range reported (labeled MSH-other in Tables 1 and 2).

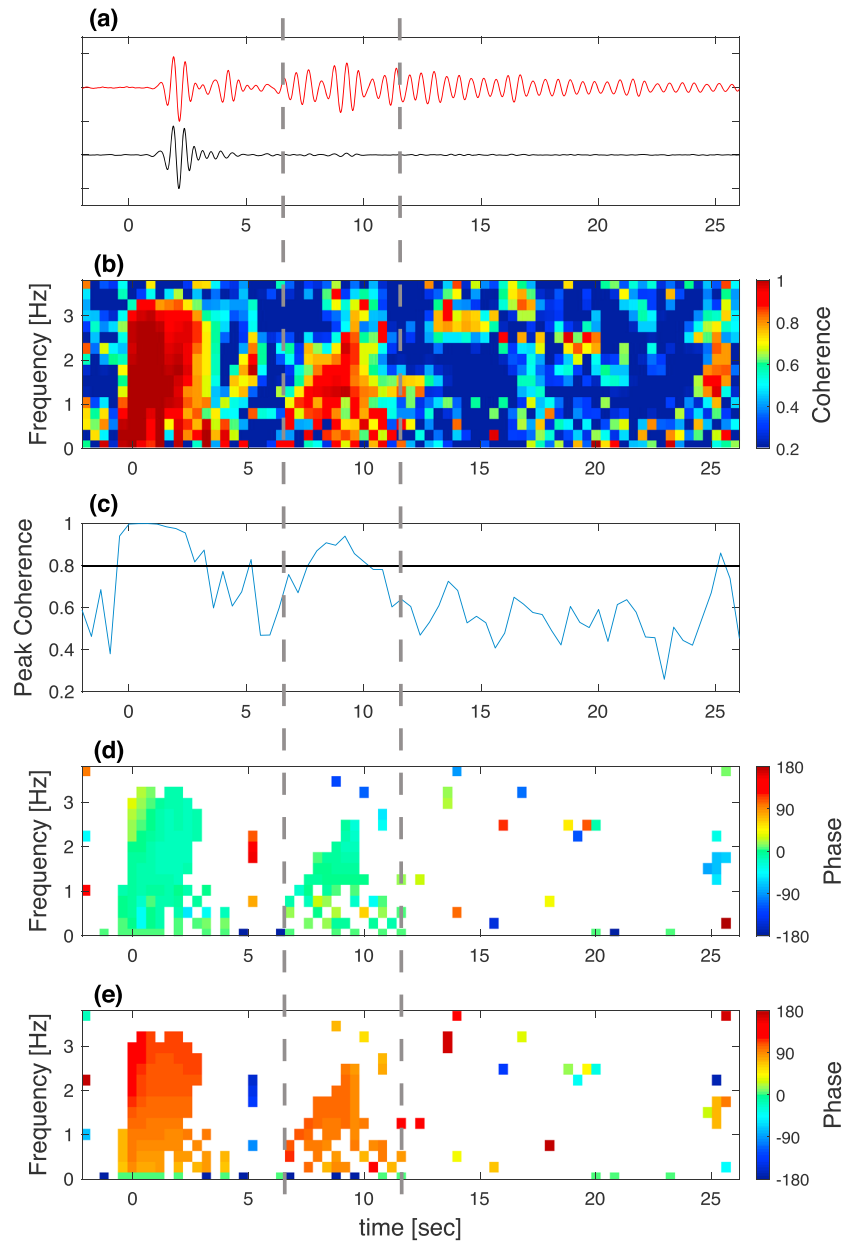


**Figure 3.** Pagan PGBF synthetic data with sensors separated by 60 m. (a) Infrasound (red) and vertical seismic (black) traces filtered from 0.5 to 3.5 Hz. (b) Coherence between synthetic infrasound and seismic data. (c) Peak coherence through time. (d) Phase between synthetic infrasound and seismic data from (a). (e) Phase found from time shifting the infrasound data until the majority of highly coherent data have a phase of  $90^\circ$ . For the coherence and phase calculations, we used a window length of 4 s with a 0.4-s step (90% overlap). The time between the vertical dashed lines highlights the airwave and GCA.

### 5.3. Mount Cleveland

We applied the GCA BAD method to two explosions from Mount Cleveland volcano detected at the CLCO seismo-acoustic station. Evaluating this method at this site is key as the infrasound sensors are deployed at various azimuths relative to the seismometer. Figure 8 shows the waveforms, coherence, and phase analysis results for CLCO and array element 5 for the first explosion on 13 December 2017. This event has high seismo-acoustic coherence above  $\sim 2$  Hz. The phase search found  $\Delta t_{90} = -0.315$  s to have the most phase values near  $90^\circ$ , which corresponds to back azimuths of  $282.2^\circ$  and  $160.0^\circ$  (Figures 9a and 9b). The phase search

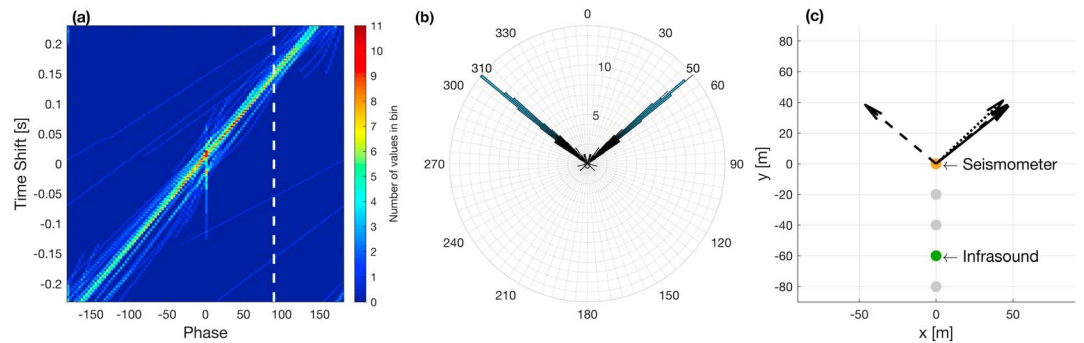


**Figure 4.** Synthetic phase search and rose diagram results. (a) Image of histogram values from each time shift ( $\Delta t$ ) searched, with  $\Delta t$  plotted on the vertical and phase on the horizontal. The color scale indicates the number of phase spectrogram values in  $3^\circ$  bins from  $-180^\circ$  to  $180^\circ$ . The vertical dotted white line highlights a phase of  $90^\circ$ . For each  $\Delta t$  there are two possible back azimuths and the number of phase values near  $90^\circ$  for each  $\Delta t$ . The number of values near  $90^\circ$  includes the totals from bins  $87^\circ$ – $90^\circ$  and  $90^\circ$ – $93^\circ$ . (c) Map view of the seismometer (orange) and infrasound microphone (green); the solid arrow shows the actual azimuth to the source, while the dashed and dotted lines show the back azimuths from the phase search (also shown in (b)) and the back azimuth from the particle motion analysis, respectively. Note that the solid arrow hides the second dashed arrow pointing to the northeast. The gray circles show the other infrasound array element locations.

(dashed arrows), particle motion determined (dotted arrow), and actual (solid arrow) back azimuths are shown in Figure 9c. At the time of maximum peak coherence, the back azimuth from the particle motion is  $281.4^\circ$ , resulting in a unique back azimuth solutions of  $282.2^\circ$  (compared to the actual back azimuth of  $283.9^\circ$ ). Figure 10 shows 1 s of 3-D displacements and the elliptical nature of the GCA particle motion, which is

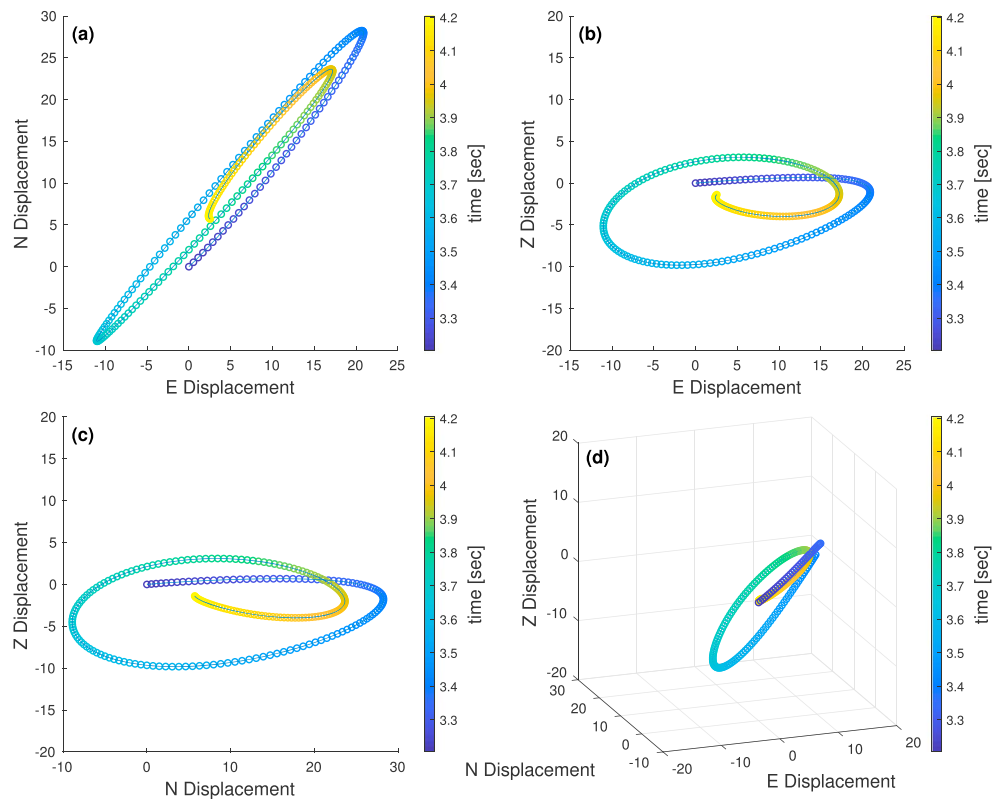


**Figure 5.** Particle motion for 1 s of a GCA recorded on the synthetic PGBF seismometer. Time is noted by the color of the circles. (a) North versus east displacement; (b) vertical versus east displacement; (c) vertical versus north displacement; (d) vertical versus north versus east displacement.

**Table 1**  
Sensor Arrangement and Back Azimuth Search Parameters

Source	$d$ (m)	$\beta$	sps (Hz)	$dt$ (s)	$\Delta t$ max (s)	$\Delta t$ step (s)	Window (s)
Synthetic	20	180°	250	0.004	0.08	0.001	4
Synthetic	40	180°	250	0.004	0.15	0.001	4
Synthetic	60	180°	250	0.004	0.23	0.001	4
Synthetic	80	180°	250	0.004	0.31	0.001	4
MSH	53.2	73.7°	40	0.025	0.175	0.0063	10
MSH-other	53.2	73.7°	40	0.025	0.175	0.0063	10
CLCO-1	20.9	183.6°	50	0.02	0.06	0.005	4
CLCO-2	122.0	301.2°	50	0.02	0.38	0.005	4
CLCO-3	158.7	52.0°	50	0.02	0.49	0.005	4
CLCO-4	176.4	106.3°	50	0.02	0.54	0.005	4
CLCO-5	211.6	221.1°	50	0.02	0.65	0.005	4
PGBF-1	4.6	44.1°	50	0.02	0.02	0.005	10
PGBF-2	84.3	321.3°	50	0.02	0.26	0.005	10
PGBF-6	87.3	11.6°	50	0.02	0.26	0.005	10

particularly notable in Figures 10b and 10d. In Figure 11, we compare the results of the coherency matrix method particle motion analysis and peak coherence through time. Without the peak coherence, it would be difficult to determine when the GCA occurred. The results for this example and the other array elements are in Tables 1 and 2 as CLCO-5; the first number identifies the infrasound array element, and the superscripted number distinguishes between the explosions: 1 for 13 December 2017 and 2 for 2 March 2018. The average difference between the GCA BAD method and the actual back azimuth across the array elements is 5.5° for the event on 13 December and 6.1° on 2 March.

#### 5.4. Mount Pagan

We applied this technique to a recorded explosion from Pagan volcano with the six array elements deployed near the seismometer at PGBF. We examine data from the pairing of the seismometer and array element 2, noted as PGBF-2 in Tables 1 and 2. Figures S2a and S2b again highlight the similarity of the seismic and infrasonic traces when filtering out the lower frequencies where the traces are not coherent. The peak coherence is not as high as in the previous cases, likely due to interference from the

seismic explosion signal, but is still above 0.8 for an ~5 s consecutively starting at 50 s (Figure S2c). Here again the time shift found in the search highlights the 90° phase, but for a narrower frequency band from ~13 to 18 Hz (Figure S2e). Figure S3a shows that the Pagan example has much fewer phase values than for the MSH example mostly due to the significantly shorter signal duration, ~30 s compared to ~1850s. Even given the lower number of values in the bins, the search finds a robust  $\Delta t_{90} = 0.005$  s and corresponding dominant back azimuths of 50° and 232° (Figure S3b). The particle motion analysis determines an azimuth of 77.7°, thus suggesting 50° as the unique solution. Figure S3c shows the seismometer and infrasonic microphone arrangement, and the solid arrow indicates the actual back azimuth to the source, 50.6°. Figure S4 shows

**Table 2**  
Back Azimuth Determination Results for the Selected Data Sets

Source	$d$ (m)	$d_0$ (m)	freq. (Hz)	Back azimuth						
				Search A	Search B	Particle motion	Result	Array processing	Actual	Difference
Synthetic	20	16.4	0.2–2.7	35.0°	325.0°	46.1°	35.0°	–	51.4°	16.4
Synthetic	40	25.5	0.2–2.7	50.4°	309.6°	46.0°	50.4°	–	51.4°	1.0
<b>Synthetic</b>	<b>60</b>	<b>38.5</b>	<b>0.2–2.7</b>	<b>50.1°</b>	<b>309.9°</b>	<b>46.0°</b>	<b>50.1°</b>	–	<b>51.4°</b>	<b>1.3</b>
Synthetic	80	50.2	0.2–2.7	51.2°	308.8°	46.3°	51.2°	–	51.4°	0.2
<b>MSH</b>	<b>53.2</b>	<b>8.6</b>	<b>5–19</b>	<b>154.5°</b>	<b>353.0°</b>	–	<b>154.5°</b>	<b>153°<sup>a</sup></b>	<b>153.6°</b>	<b>–0.9</b>
MSH-other	53.2	19.3	4–19	322.5°	185.0°	–	185.0°	185°–190° <sup>a</sup>	–	–
CLCO-1 <sup>b</sup>	20.9	0.0	1.5–24	273.6°	93.6°	277.3°	273.6°	283.8°	283.9°	10.3
CLCO-2 <sup>b</sup>	122.0	113.8	1.5–24	322.5°	280.0°	281.4°	280.0°	283.8°	283.9°	3.9
CLCO-3 <sup>b</sup>	158.7	107.3	1.5–24	279.5°	184.5°	281.2°	279.5°	283.8°	283.9°	4.4
CLCO-4 <sup>b</sup>	176.4	175.5	1.5–24	296.1°	276.5°	281.9°	276.5°	283.8°	283.9°	7.4
<b>CLCO-5<sup>b</sup></b>	<b>211.6</b>	<b>102.4</b>	<b>1.5–24</b>	<b>282.2°</b>	<b>160.0°</b>	<b>288.0°</b>	<b>282.2°</b>	<b>283.8°</b>	<b>283.9°</b>	<b>1.7</b>
CLCO-1 <sup>c</sup>	20.9	1.6	1.9–22	89.1°	278.1°	273.2°	278.1°	284°	283.9°	5.8
CLCO-2 <sup>c</sup>	122.0	110.5	1.9–19	326.4°	276.1°	272.5°	276.1°	284°	283.9°	7.8
CLCO-3 <sup>c</sup>	158.7	104.0	1.9–22	281.1°	182.9°	272.4°	281.1°	284°	283.9°	2.8
CLCO-4 <sup>c</sup>	176.4	170.6	1.9–22	301.0°	271.6°	272.4°	271.6°	284°	283.9°	12.3
CLCO-5 <sup>c</sup>	211.6	102.4	1.9–22	282.2°	160.0°	272.5°	282.2°	284°	283.9°	1.7
PGBF-1	4.6	3.4	13–24	86.0°	2.3°	77.7°	86.0°	51°	50.6°	–35.4
PGBF-2	84.3	1.7	13–24	50.2°	232.5°	77.7°	50.2°	51°	50.6°	0.4
PGBF-6	87.3	61.7	13–24	56.6°	326.6°	77.7°	56.6°	51°	50.6°	–6.0

Note. Search A and B are the two possible back azimuths determined from the phase search. Particle motion is the back azimuth determined from the coherency matrix method used to pick a unique back azimuth. Result is the final back azimuth determined from our GCA BAD method. Array processing is the back azimuth determined from independent array processing. Actual is the back azimuth calculated given the seismometer and source locations. Difference is the difference between the actual back azimuth and the result from the GCA BAD method. Examples in bold text have figures included.

<sup>a</sup>From Matoza and Fee (2014). <sup>b</sup>Event on 13 December 2017. <sup>c</sup>Event on 2 March 2018.

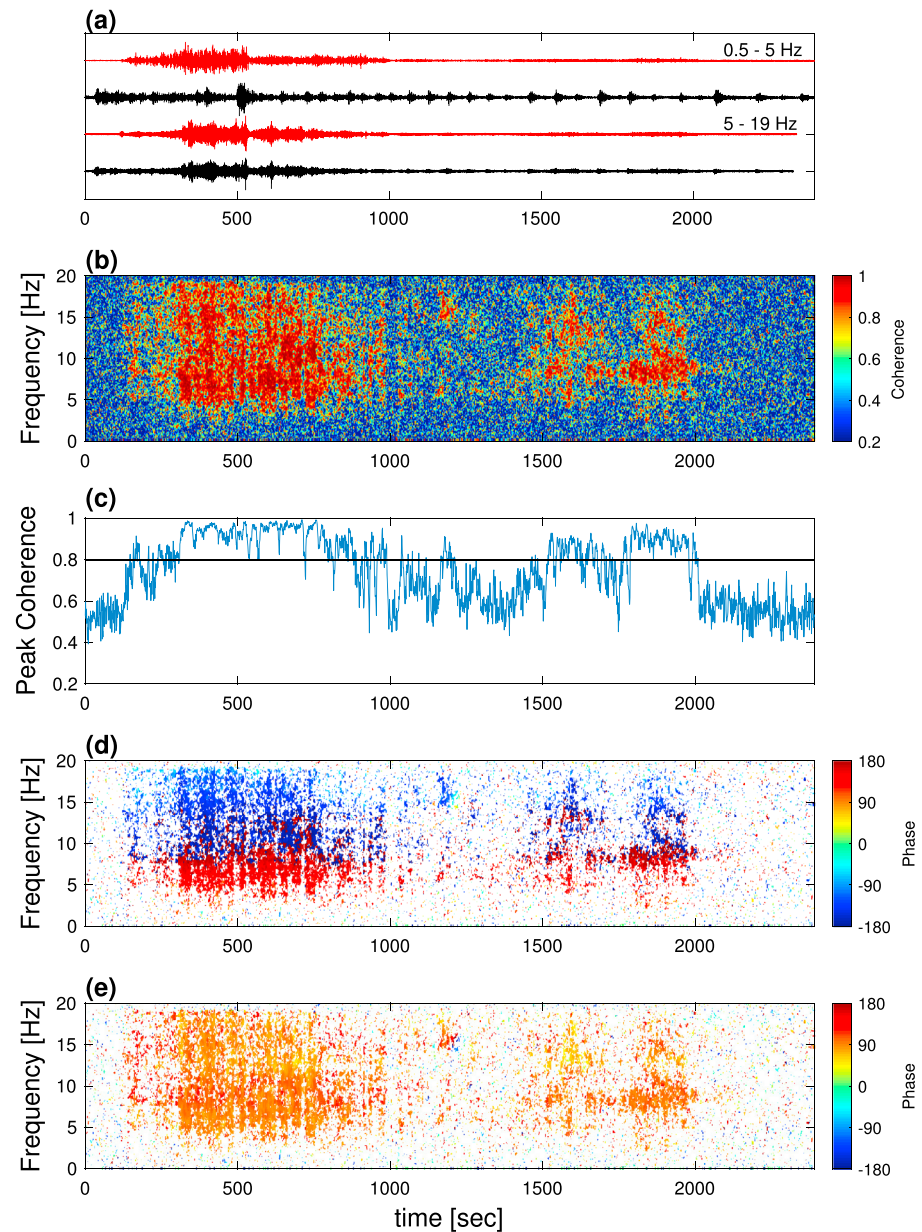


**Figure 6.** Mount St. Helens coherence and phase. (a) Infrasound (red) and vertical seismic (black) traces filtered from 0.5 to 5 Hz (top) and 5 to 19 Hz (bottom). (b) Coherence of infrasound and seismic data. (c) Peak coherence through time. (d) Phase between same infrasound and seismic data as in (b). (e) Phase found from time shifting the infrasound data until the majority of highly coherent data have a phase of  $90^\circ$ . For the coherence and phase calculations, we used a window length of 10 s with a 1-s step (90% overlap).

1 s of particle motion starting at 51 s, the time of maximum peak coherence. The particle motion is clearly elliptical, particularly in Z versus E and N versus E (Figures S4b and S4d).

We further apply our method to the other array elements at PGBF. Array element 1, PGBF-1,  $\sim 4.6$  m from the seismometer, had a very coarse result, in that from one time step to the next was about a  $30^\circ$  change in azimuth and was  $\sim 34^\circ$  off from the actual back azimuth. The pairing with array element 6 (PGBF-6), about the same distance from the seismometer as element 2, gives a back azimuth of  $56^\circ$ . The infrasonic array deployed with PGBF has three additional elements  $\sim 160$  m from the seismometer. We tried our method with each of those elements, but they failed to find a robust back azimuth as the peak coherence was below the 0.8 threshold. Infrasound array processing of this event using a least squares technique yields a back azimuth

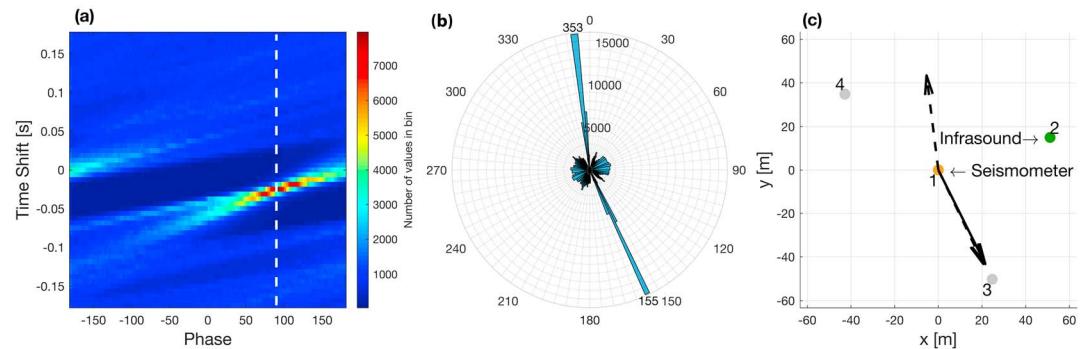


**Figure 7.** Mount St. Helens phase search and rose diagram result, similar to the synthetic example in Figure 4. (a) Image of histogram values from each time shift. (b) Rose diagram of the two possible back azimuths and the number of phase values near  $90^\circ$  for each time shift. (c) The arrangement of the seismometer (orange) and infrasound microphone (green); the solid arrow shows the actual azimuth to the source, while the dashed lines show the back azimuths from the phase search (also shown in (b)). The gray circles show the other microphone locations. One of the two primary back azimuths in (b) agrees well with the actual back azimuth in (c).

of  $\sim 51^\circ$ . See Tables 1 and 2 for summaries of sensor arrangements, search parameters, and results. The bold text indicates the examples for which figures are included (Table 2).

## 6. Discussion

In general, we find that our GCA BAD method works well for the examples examined here, especially given the variation in coherence from near perfect (noise-added synthetic) to marginal (Pagan). For the successful cases, the actual and resulting back azimuths differ on average by  $5.0^\circ$  with a standard deviation of  $4.6^\circ$ . Our GCA BAD method also provides a better result than the particle motion analysis alone. Particle motion analysis has been shown to be a rough estimator for back azimuth (Montalbetti & Kanasevich, 1970; Vidale, 1986) and applied here it works well as a tool to distinguish between the nonunique search results. In the case where the back azimuth is not found (PGBF-1), we attribute this failure to the sensor spacing being too small for the respective sample rate. Below we discuss the limitations and application of the GCA BAD method and suggest future work.

### 6.1. Practicalities of Application

#### 6.1.1. Sensor Spacing and Measuring Sensor Locations

Sufficient spacing between the seismic and infrasound sensor and highly accurate sensor locations are key to the success of the GCA BAD method. We have found that the sensors need to be separated by at least the equivalent distance a sound wave travels between recorded samples ( $dt$ , or  $1/(\text{sample rate})$ ). In other words,  $d$  needs to be at least  $dt \times c$ ; otherwise, the phase delay above  $90^\circ$  is unresolvable. Since our method relies on time shifting the data, if the sensors are deployed at less than a  $dt$  equivalent distance, then all the time shifts will be subsample rate. With sub- $dt$  equivalent sensor spacing an accurate back azimuth is not feasible, but an evaluation of the seismo-acoustic coherence is still a valuable tool as it can be used to distinguish GCAs and acoustic waves in the seismic record (Fee et al., 2017; Matoza & Fee, 2014). We recommend a sensor spacing of at least a  $dt$  equivalent, if not several, and as high a sample rate as is feasible. Further details of the sensitivity of the GCA BAD method with respect to sensor spacing and critical angle criteria may be found in supporting information section S4 and Figure S6.

Increased sensor spacing will also decrease the coherence and potentially the effectiveness of the method. In applying the GCA BAD method with each array element at PGBF, the lower coherence at the further array elements,  $d = \sim 160$  m, limited the accuracy of the back azimuth estimate. In contrast, the Mount Cleveland examples worked well with a sensor separation out to  $\sim 210$  m. Investigations on coherence loss across infrasonic array elements found that a decrease in SNR has a more significant impact on coherence loss than sensor spacing (Christie & Campus, 2009; Green, 2015). The high coherence out to  $\sim 210$  m in the Cleveland examples is likely due to high SNR. For frequencies of 0.1–1 Hz, coherence remains high within 0.5 km sensor spacing and coherence loss is higher parallel to the wavefront than perpendicular to it (Christie & Campus,

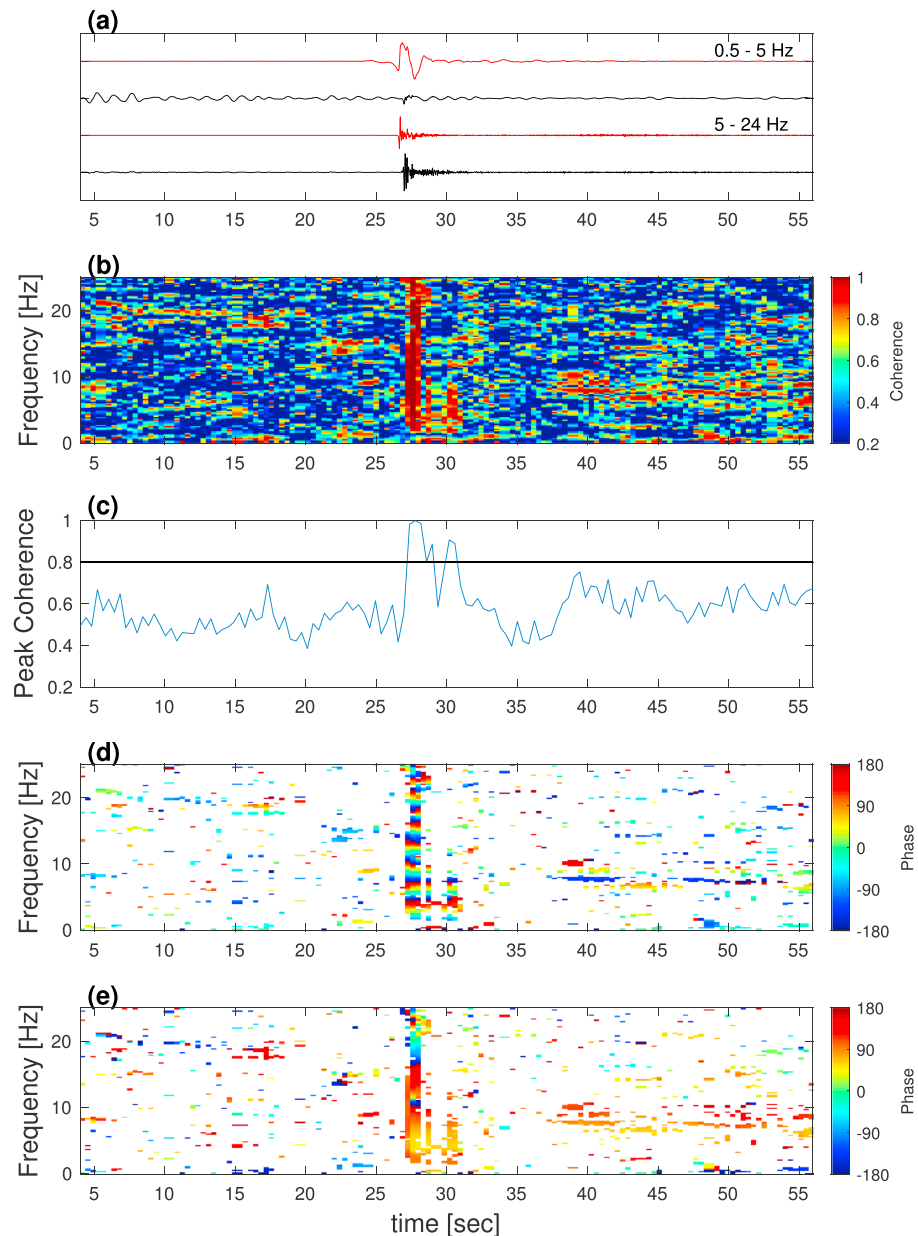


**Figure 8.** Cleveland CLCO coherence and phase. (a) Infrasound (red) and vertical seismic (black) traces filtered from 0.5 to 5 Hz (top) and 5 to 24 Hz (bottom). (b) Coherence of infrasound and seismic data. (c) Peak coherence through time. (d) Phase between same high-pass filtered infrasound and seismic data as in (b). (e) Phase found from time shifting the infrasound data until the majority of highly coherent data have a phase of  $90^\circ$ . For the coherence and phase calculations, we used a window length of 4 s with a 0.4-s step (90% overlap).

2009; Green, 2015). As GCA are usually observed at frequencies an order of magnitude higher than these studies, 1–20+ Hz, the spatial coherence range is likely less than observed by Green (2015). The sensor spacing of  $\sim 85$  m, in the cases of PGBF-2 and PGBF-6, is about an order of magnitude lower than the 0.5 km spacing found in (Green, 2015). We suggest a maximum sensor spacing of  $\sim 100$  m, but  $\sim 50$  m is likely better to maintain high coherence for waves arriving from a variety of back azimuths and with varying SNR. Local topographic features may also influence seismo-acoustic coherence (Nishida & Ichihara, 2015). Further investigation into spatial coherence loss at higher frequencies and due to topography is needed to improve this recommendation.

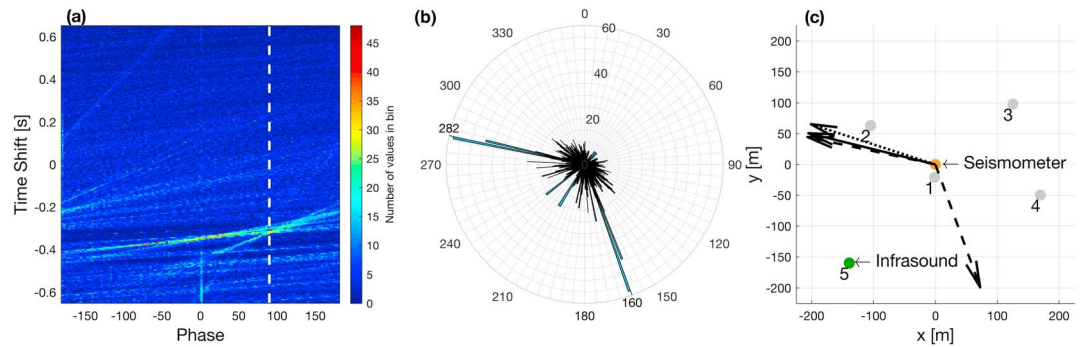


**Figure 9.** Cleveland CLCO search and rose diagram result, similar to Figures 4 and 7. (a) Image of histogram values from each time shift. (b) Rose diagram of the two possible back azimuths and the number of phase values near 90° for each time shift. (c) The arrangement of the seismometer (orange) and infrasound microphone (green); the solid arrow shows the actual azimuth to the source, while the dashed and dotted lines show the back azimuths from the phase search (also shown in (b)) and the back azimuth from the particle motion analysis, respectively. The gray circles show the other infrasound array element locations. Note that one of the two back azimuth results in (b) is consistent with the actual back azimuth in (c).

Highly accurate sensor locations are also key to the success of our method. For the MSH case, we compared GCA BAD method results when using sensor locations from handheld and differential Global Positioning System (GPS) coordinates and the *x-y* distances reported in Matoza and Fee (2014) from the seismometer to the infrasonic microphone. The differential GPS used had an accuracy of 50 cm (Matoza et al., 2007), where handheld GPS's typically have 1–5 m precision in open areas with an unobstructed view of satellites (Johnson & Barton, 2004). Application of the GCA BAD method with the handheld GPS coordinates gave a back azimuth of ~158°, which was improved by ~3° when we used the reported *x-y* distances and then by an additional degree, ~154°, using the differential GPS coordinates. This confirms the importance of obtaining highly

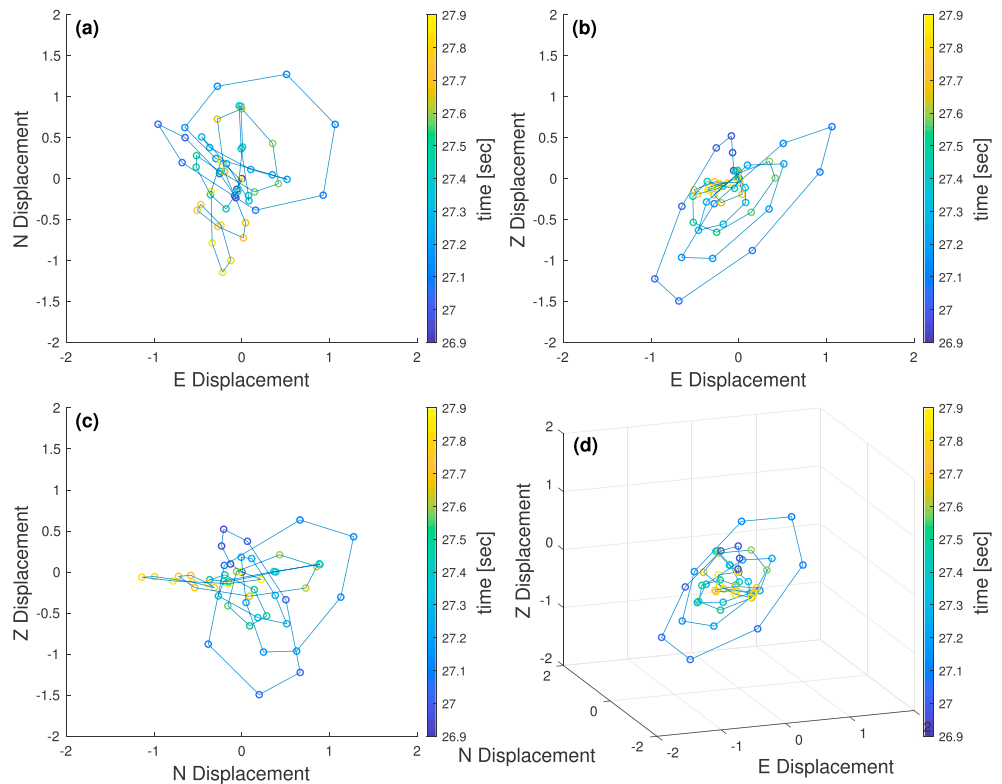


**Figure 10.** Particle motion for 1 s of a GCA recorded on CLCO seismometer. The data are filtered from 5 to 24 Hz as are shown in Figure 8a. Time is noted by the color of the circles. (a) North versus east displacement; (b) vertical versus east displacement; (c) vertical versus north displacement; (d) vertical versus north versus east displacement.

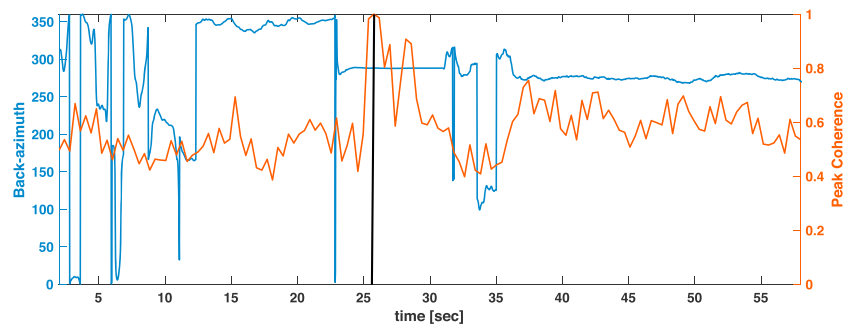


**Figure 11.** Comparison of back azimuth from particle motion (blue line) determined using the coherency matrix method and peak coherence through time (orange line) for the same period of data shown in Figure 8. The vertical black line highlights the time of peak coherence and the corresponding particle motion back azimuth.

accurate GPS coordinates, and if those are not available we suggest physically measuring the  $x$ - $y$  distances from seismometer to microphone.

### 6.1.2. Source Distance and Altitude

In the application of the GCA BAD method we assume an incidence angle near  $90^\circ$  from vertical, as our sound waves arrive from local ( $< \sim 15$  km) distances (Ben-Menahem & Singh, 2000; Fee & Matoza, 2013). Edwards et al. (2007) observed the airwave and GCA across a seismo-acoustic array from the shockwave resulting from atmospheric reentry of the Stardust sample return capsule. They documented retrograde particle motion and a coherent GCA, suggesting that our method could be applied to an infrasonic source at any altitude. Applying this GCA method to global infrasound monitoring efforts would be advantageous as the current network of arrays deployed is sparse. For the examples we investigated, the sources are at local distances such that the arrivals are likely direct and near  $90^\circ$  from vertical. When an infrasound wave arrives at the Earth's surface after being refracted near the tropopause, stratopause, or mesopause it can have a lower incidence angle than near  $90^\circ$  (Fee & Matoza, 2013). When this refracted wave travels across an infrasound array it will have a higher apparent (trace) velocity than the speed of sound due to the nonhorizontal angle of incidence. Common trace velocities and incidence angles relative to vertical for the different arrivals are 343 m/s and  $\sim 90^\circ$  for tropospheric, 330–350 m/s and  $< 79^\circ$  for stratospheric, and 400 m/s and  $60^\circ$  m/s for thermospheric with a sound speed at the surface of 343 m/s (Fee et al., 2013; Matoza et al., 2011). These incidence angles suggest that the GCA BAD method would work for long-range infrasound, especially those ducted in the troposphere and stratosphere. Further investigation is needed to determine the effect of incidence angle on the GCA BAD method presented here.

Timing between the seismic and infrasonic arrivals is also key in determining the GCA back azimuth. In comparing the Pagan and MSH examples we note that while the GCA method successfully determined back azimuths for both, the Pagan data have lower coherence, hovering just over and under our threshold. This may be due to the presence of pure seismic phases even at higher frequencies. The PGBF array is  $\sim 3$  km from the source. If the explosion wave travels at 5 km/s through the ground and 340 m/s through the atmosphere, the airwave will arrive  $\sim 8.2$  s after the seismic wave. Since the explosion signal is  $\sim 30$  s in duration, the seismic explosion signal and the GCA will overlap, thus lowering the coherence during the GCA. This suggests that deploying seismo-acoustic sensor pairs further from potential sources may enhance the GCA BAD method's effectiveness, but further investigation is needed.

### 6.1.3. Seismometer Characteristics and Deployment Depth

The examples presented in this manuscript employed three-component broadband seismometers, buried near the surface, as opposed to short period or borehole seismometers. Recent work has shown a borehole seismometer recorded GCA signals from Sakurajima Volcano, Japan (Ichiara, 2016). However, Ichiara (2016) reports that the borehole data (98 m depth) and surface infrasound data did not correlate well. This suggests that our method may not work with seismometers buried at borehole depths, but further investigation is needed. While the seismic data set we used was broadband, data from short-period seismometers should also work. The examples of GCAs in this manuscript and in Matoza and Fee (2014) are higher in frequency, above 5 Hz. There are, however, examples of energy at lower frequencies, such as the recent

Pavlof Volcano eruption where there was coherence from  $\sim 0.8$  to 8 Hz (Fee et al., 2017). In general, the frequency characteristics of GCAs reflect those of the incident airwave (Edwards et al., 2007, 2008). Much of the GCA energy in the Pavlof eruption would likely have been recorded on a short-period ( $\sim 1$  s) seismometer as well. The key characteristic of the seismometer is that it should be three-component to utilize the particle motion to resolve a unique back azimuth.

## 6.2. Future Directions and Recommendations

The GCA BAD method presented here could be applied to any seismo-acoustic pair, assuming that the critical angle criteria (supporting information, section S4) have been met. Two suggested future research directions for this method that have yet to be explored in detail are application to long-range infrasound and explosion source location. Our method determines the back azimuth to a local infrasonic source. A desired next step is to resolve a source location. If nearly collocated seismo-acoustic sensor pairs were strategically deployed across a region, the GCA method could be applied at each pair and the back azimuth used to triangulate a source location. Many seismic deployments include an infrasound sensor with each seismometer. Data from such deployments would be ideal for evaluating if the GCA BAD method works on a global scale. The GCA method could also be used to monitor volcanic activity on a regional scale. If seismo-acoustic sensor pairs were deployed throughout a volcanic region, as they increasingly are, with sensors spaced at several  $dt$ -equivalent lengths, coherence could be used to detect GCAs, indicating an acoustic source. The GCA method would then determine the back azimuth, which could be linked to a known volcanic source. With a full seismo-acoustic network, triangulation could be used to determine which volcano is active at a given moment. Another potential application, with some adaptation to this method, is determining time-varying back azimuths. This would be of value in certain situations where the source migrates, such as during fissure eruptions or where multiple vents may be active.

A logical data set to apply this method to is the EarthScope TA; unfortunately, the seismic sensor and infrasound sensor at each site appear too close together. For TA deployments that have become permanent state or federal stations or any other seismo-acoustic deployments, it would be advantageous to move the infrasound microphone away from the seismometer by  $\sim 50$  m and increase the sampling rate. Accurate reporting of relative station locations would also be important. These stations could then be used to detect and determine back azimuths to myriad acoustic sources. Edwards et al. (2007) examined the local soil properties to estimate the local seismic velocity and energy coupling efficiency. A variety of deployments across a large region, such as the United States, with documentation of local geology and soil characteristics would allow for further investigation into factors that influence acoustic energy coupling to the ground. For seismic studies this could improve seismometer site selection in order to avoid geologic settings where acoustic energy more easily couples into the ground.

## 7. Conclusion

In this manuscript we present a method to robustly determine the back azimuth to an infrasonic source using only one infrasonic microphone and one nearly collocated three-component seismometer. The method exploits the phase difference between the infrasonic wave and GCA, along with the GCA particle motion, to determine a unique back azimuth to the source. We observe high coherence between airwaves and GCAs from synthetic and volcanic sources. We test the technique using a synthetic data set and apply it with success to three volcanic data sets with variable SNR and orders of magnitude difference in signal duration. Our GCA BAD method generally finds back azimuths that are on average within  $5.0^\circ$  of the actual and the array processing determined back azimuths, yet uses substantially less sensors and resources than traditional infrasound arrays. Key elements to successfully using this method are (1) separating the seismometer and infrasonic microphone by several  $dt$ -equivalent lengths (the distance traveled by an acoustic wave during one digitized sample), but less than 100 m; (2) acquiring data at a high sample rate (e.g.,  $> 100$  Hz); and (3) using a three-component seismometer. Sensors separated by less than a  $dt$ -equivalent distance could still be used to detect acoustic sources, but a back azimuth will not be successfully determined. This GCA BAD technique could be used to detect and help locate explosive acoustic sources, such as those from volcanoes and anthropogenic explosions. Future work should explore the optimal sensor separation distances and application to long-range acoustics sources.

## Acknowledgments

We extend thanks to the Geophysical Institute of the University of Alaska Fairbanks and NSF EAR-1331084, EAR-1614323, and EAR-1614855 for support of this work. Mike West, Carl Tape, and Curt Szuberla provided helpful comments on the method and results. The MSH data under station name MSH21 are available upon request from Natural Resources Canada. Requests can be made manually by contacting nrcan.lms.mchisit.nrcan@canada.ca or through the autodrm service ([http://www.earthquakescanada.nrcan.gc.ca/stdon/AutoDRM/autodrm\\_req-en.php](http://www.earthquakescanada.nrcan.gc.ca/stdon/AutoDRM/autodrm_req-en.php); <https://doi.org/10.7914/SN/CN>). The Mt. Pagan seismo-acoustic and Mt. Cleveland acoustic data are available in the supporting information. Mt. Cleveland seismic data are available through the IRIS DMC under network AV and station CLCO.

## References

- Aki, K., & Richards, P. G. (2002). Plane waves in homogeneous media and their reflection and transmission at a plane boundary. In J. Ellis (Ed.), *Quantitative seismology* (pp. 155–156). Sausalito, CA: University Science Books.
- Ben-Menahem, A., & Singh, S. J. (2000). *Seismic waves and sources* (2nd ed.). New York: Springer. <https://doi.org/10.1007/978-1-4612-5856-8>
- Cansi, Y. (1995). An automatic seismic event processing for detection and location: The P.M.C.C. Method. *Geophysical Research Letters*, *22*(9), 1021–1024. <https://doi.org/10.1029/95GL00468>
- Cansi, Y., & Klinger, Y. (1997). An automated data processing method for mini-arrays. *Newsletter of the European-Mediterranean Seismological Center*, *11*, 2–4.
- Christie, D. R., & Campus, P. (2009). The IMS infrasound network: Design and establishment of infrasound stations. In *Infrasound monitoring for atmospheric studies* (pp. 29–75). Netherlands: Springer. [https://doi.org/10.1007/978-1-4020-9508-5\\_2](https://doi.org/10.1007/978-1-4020-9508-5_2)
- De Angelis, S., Fee, D., Haney, M., & Schneider, D. (2012). Detecting hidden volcanic explosions from Mt. Cleveland Volcano, Alaska, with infrasound and ground-coupled airwaves. *Geophysical Research Letters*, *39*, L21312. <https://doi.org/10.1029/2012GL053635>
- Edwards, W. N., Eaton, D. W., & Brown, P. G. (2008). Seismic observations of meteors: Coupling theory and observations. *Reviews of Geophysics*, *46*, RG4007. <https://doi.org/10.1029/2007RG000253>
- Edwards, W. N., Eaton, D. W., McCausland, P. J., ReVelle, D. O., & Brown, P. G. (2007). Calibrating infrasonic to seismic coupling using the Stardust sample return capsule shockwave: Implications for seismic observations of meteors. *Journal of Geophysical Research*, *112*, B10306. <https://doi.org/10.1029/2006JB004621>
- Fee, D., Haney, M. M., Matoza, R., Szuberla, C. A. L., Lyons, J., & Waythomas, C. (2016). Seismic envelope-based detection and location of ground-coupled airwaves from volcanoes in Alaska. *Bulletin of the Seismological Society of America*, *106*(3), 1024–1035. <https://doi.org/10.1785/0120150244>
- Fee, D., Haney, M. M., Matoza, R. S., Van Eaton, A. R., Cervelli, P., Schneider, D. J., & Iezzi, A. M. (2017). Volcanic tremor and plume height hysteresis from Pavlof Volcano, Alaska. *Science*, *355*(6320), 45–48. <https://doi.org/10.1126/science.aah6108>
- Fee, D., & Matoza, R. S. (2013). An overview of volcano infrasound: From hawaiian to plinian, local to global. *Journal of Volcanology and Geothermal Research*, *249*, 123–139. <https://doi.org/10.1016/j.jvolgeores.2012.09.002>
- Fee, D., McNutt, S. R., Lopez, T. M., Arnoult, K. M., Szuberla, C. A. L., & Olson, J. V. (2013). Combining local and remote infrasound recordings from the 2009 Redoubt Volcano eruption. *Journal of Volcanology and Geothermal Research*, *259*(C), 100–114. <https://doi.org/10.1016/j.jvolgeores.2011.09.012>
- Green, D. N. (2015). The spatial coherence structure of infrasonic waves: Analysis of data from International Monitoring System arrays. *Geophysical Journal International*, *201*(1), 377–389. <https://doi.org/10.1093/gji/ggu495>
- Haney, M. M., van Wijk, K., Preston, L. A., & Aldridge, D. F. (2009). Observation and modeling of source effects in coda wave interferometry at Pavlof volcano. *The Leading Edge*, *28*(5), 554–560. <https://doi.org/10.1190/1.3124930>
- Ichihara, M. (2016). Seismic and infrasonic eruption tremors and their relation to magma discharge rate: A case study for sub-Plinian events in the 2011 eruption of Shinmoe-dake, Japan. *Journal of Geophysical Research: Solid Earth*, *121*, 7101–7118. <https://doi.org/10.1002/2016JB013246>
- Ichihara, M., Takeo, M., Yokoo, A., Oikawa, J., & Ohminato, T. (2012). Monitoring volcanic activity using correlation patterns between infrasound and ground motion. *Geophysical Research Letters*, *39*, L04304. <https://doi.org/10.1029/2011GL050542>
- Johnson, C. E., & Barton, C. C. (2004). Where in the world are my field plots? Using GPS effectively in environmental field studies. *Frontiers in Ecology and the Environment*, *2*(9), 475–482. <https://doi.org/10.2307/3868336>
- Johnson, J. B., & Malone, S. D. (2007). Ground-coupled acoustic airwaves from Mount St. Helens provide constraints on the May 18, 1980 eruption. *Earth and Planetary Science Letters*, *258*(1–2), 16–31. <https://doi.org/10.1016/j.epsl.2007.03.001>
- Jurkevics, A. (1988). Polarization analysis of three-component array data. *Bulletin of the Seismological Society of America*, *78*(5), 1725–1743.
- Langston, C. A. (2004). Seismic ground motions from a bolide shock wave. *Journal of Geophysical Research*, *109*, B12309. <https://doi.org/10.1029/2004JB003167>
- Lee, D.-C., Olson, J. V., & Szuberla, C. A. L. (2013). Computationally robust and noise resistant numerical detector for the detection of atmospheric infrasound. *The Journal of the Acoustical Society of America*, *134*(1), 862–868. <https://doi.org/10.1121/1.4807802>
- Lyons, J. J., Haney, M. M., Fee, D., & Paskievitch, J. F. (2014). Distinguishing high surf from volcanic long-period earthquakes. *Geophysical Research Letters*, *41*, 1171–1178. <https://doi.org/10.1002/2013GL058954>
- Lyons, J. J., Haney, M. M., Werner, C., Kelly, P., Patrick, M., Kern, C., & Trusdell, F. (2016). Long period seismicity and very long period infrasound driven by shallow magmatic degassing at Mount Pagan, Mariana Islands. *Journal of Geophysical Research: Solid Earth*, *121*, 188–209. <https://doi.org/10.1002/2015JB012490>
- Madshus, C., Løvholt, F., Kaynia, A., Hole, L., Attenborough, K., & Taherzadeh, S. (2005). Air-ground interaction in long range propagation of low frequency sound and vibration-field tests and model verification. *Applied Acoustics*, *66*(5), 553–578. <https://doi.org/10.1016/j.apacoust.2004.09.006>
- Matoza, R. S., & Fee, D. (2014). Infrasonic component of volcano-seismic eruption tremor. *Geophysical Research Letters*, *41*, 1964–1970. <https://doi.org/10.1002/2014GL059301>
- Matoza, R. S., Fee, D., Green, D. N., le Pichon, A., Vergoz, J., Haney, M. M., et al. (2018). Local, regional, and remote seismo-acoustic observations of the April 2015 VEI 4 eruption of Calbuco Volcano, Chile. *Journal of Geophysical Research: Solid Earth*, *123*, 3814–3827. <https://doi.org/10.1002/2017JB015182>
- Matoza, R. S., Garcés, M. A., Chouet, B. A., D'Auria, L., Hedlin, M. A. H., De Groot Hedlin, C., & Waite, G. P. (2009). The source of infrasound associated with long-period events at Mount St. Helens. *Journal of Geophysical Research*, *114*, B04305. <https://doi.org/10.1029/2008JB006128>
- Matoza, R. S., Hedlin, M. A. H., & Garcés, M. A. (2007). An infrasound array study of Mount St. Helens. *Journal of Volcanology and Geothermal Research*, *160*(3–4), 249–262. <https://doi.org/10.1016/j.jvolgeores.2006.10.006>
- Matoza, R. S., le Pichon, A., Vergoz, J., Herry, P., Lalande, J.-M., Lee, H.-i., et al. (2011). Infrasonic observations of the June 2009 Sarychev Peak eruption, Kuril Islands: Implications for infrasonic monitoring of remote explosive volcanism. *Journal of Volcanology and Geothermal Research*, *200*(1–2), 35–48. <https://doi.org/10.1016/j.jvolgeores.2010.11.022>
- Montalbetti, J. F., & Kanasevich, E. R. (1970). Enhancement of teleseismic body phases with a polarization filter. *Geophysical Journal of the Royal Astronomical Society*, *21*(2), 119–129. <https://doi.org/10.1111/j.1365-246X.1970.tb01771.x>
- Neuberg, J., & Pointer, T. (2000). Effects of volcano topography on seismic broad-band waveforms. *Geophysical Journal International*, *143*(1), 239–248. <https://doi.org/10.1046/j.1365-246x.2000.00251.x>

- Nishida, K., & Ichihara, M. (2015). Real-time infrasonic monitoring of the eruption at a remote island volcano using seismoacoustic cross correlation. *Geophysical Journal International*, *204*(2), 748–752. <https://doi.org/10.1093/gji/ggv478>
- Olson, J. V., & Szuberla, C. A. (2008). Processing infrasonic array data. In D. Havelock, S. Kuwano, & M. Vorlander (Eds.), *Handbook of signal processing in acoustics* (pp. 1487–1496). New York: Springer.
- Olson, J. V., & Szuberla, C. A. L. (2005). Distribution of wave packet sizes in microbarom wave trains observed in Alaska. *The Journal of the Acoustical Society of America*, *117*(3), 1032–1037. <https://doi.org/10.1121/1.1854651>
- Shields, D. F. (2005). Low-frequency wind noise correlation in microphone arrays. *The Journal of the Acoustical Society of America*, *117*(6), 3489–3496. <https://doi.org/10.1121/1.1879252>
- Smart, E., & Flinn, E. A. (1971). Fast frequency-wavenumber analysis and Fisher signal detection in real-time infrasonic array data processing. *Geophysical Journal International*, *26*(1–4), 279–284. <https://doi.org/10.1111/j.1365-246X.1971.tb03401.x>
- Smith, C. M., McNutt, S. R., & Thompson, G. (2016). Ground-coupled airwaves at Pavlof Volcano, Alaska, and their potential for eruption monitoring. *Bulletin of Volcanology*, *78*(7), 1–12. <https://doi.org/10.1007/s00445-016-1045-0>
- Tauzin, B., Debayle, E., Quantin, C., & Coltice, N. (2013). Seismoacoustic coupling induced by the breakup of the 15 February 2013 Chelyabinsk meteor. *Geophysical Research Letters*, *40*, 3522–3526. <https://doi.org/10.1002/grl.50683>
- Thelen, W. A., & Cooper, J. (2015). An analysis of three new infrasound arrays around Kilauea Volcano Rep. 2014-1253.
- Vidale, J. E. (1986). Complex polarization analysis of particle motion. *Bulletin of the Seismological Society of America*, *76*(5), 1393–1405.
- Walker, K. T., Hedlin, M. A. H., De Groot Hedlin, C., Vergoz, J., Le Pichon, A., & Drob, D. P. (2010). Source location of the 19 February 2008 Oregon bolide using seismic networks and infrasound arrays. *Journal of Geophysical Research*, *115*, B12329. <https://doi.org/10.1029/2010JB007863>
- Wang, H., & Kaveh, M. (1985). Coherent signal-subspace processing for the detection and estimation of angles of arrival of multiple wide-band sources. *IEEE Transactions on Acoustics, Speech, and Signal Processing*, *33*(4), 823–831. <https://doi.org/10.1109/TASSP.1985.11164667>
- Wilson, K. D., Greenfield, R. J., & White, M. J. (2007). Spatial structure of low-frequency wind noise. *The Journal of the Acoustical Society of America*, *122*(6), EL223–EL228. <https://doi.org/10.1121/1.2786608>